

Article

# Heat Transfer in a Drilling Fluid with Geothermal Applications

Wei-Tao Wu <sup>1</sup>, Nadine Aubry <sup>2</sup>, James F. Antaki <sup>1</sup>, Mark L. McKoy <sup>3</sup> and Mehrdad Massoudi <sup>4,\*</sup>

<sup>1</sup> Department of Biomedical Engineering, Carnegie Mellon University, Pittsburgh, PA 15213, USA; weitaow@andrew.cmu.edu (W.-T.W.); antaki@andrew.cmu.edu (J.F.A.)

<sup>2</sup> Department of Mechanical and Industrial Engineering, Northeastern University, Boston, MA 02115, USA; n.aubry@northeastern.edu

<sup>3</sup> U.S. Department of Energy, National Energy Technology Laboratory (NETL), 3610 Collins Ferry Road, Morgantown, WV 26507-0880, USA; mark.mckoy@netl.doe.gov

<sup>4</sup> U.S. Department of Energy, National Energy Technology Laboratory (NETL), 626 Cochran Mill Road, Pittsburgh, PA 15236-0940, USA

\* Correspondence: mehrdad.massoudi@netl.doe.gov; Tel.: +1-412-386-4975

Received: 14 July 2017; Accepted: 1 September 2017; Published: 6 September 2017

**Abstract:** The effects of various conditions on the fluid flow, particle migration and heat transfer in non-linear fluids encountered in drilling and geothermal applications are studied. We assume that the drilling fluid is a suspension composed of various substances, behaving as a non-linear complex fluid, where the effects of particle volume fraction, shear rate, and temperature on the viscosity and thermal diffusivity are considered. The motion of the particles is described using a concentration flux equation. Two problems are studied: flow in a vertical pipe and flow between two (eccentric) cylinders where the inner cylinder is rotating. We consider effects of earth temperature, the rotational speed of the inner cylinder, and the bulk volume fraction on the flow and heat transfer.

**Keywords:** geothermal energy; drilling fluid; concentrated suspension; heat transfer; non-Newtonian fluids; non-homogeneous fluids; rheology

## 1. Introduction

Drilling is an essential aspect of many geothermal energy applications (see Younger [1]). It allows the capture of high-density thermal energy stored in the deep Earth [2]. The fluid, which flows in the well during the drilling operation is called the drilling fluid/mud, which is a solid-fluid suspension composed of particles in a fluid. Geothermal energy is the thermal energy generated and stored in the Earth which can be extracted and used [3]. Similar to other natural energy resources, such as sunlight, wind, rain, tides, and waves, geothermal energy is also considered as a renewable or semi-renewable source of energy [4,5]. This is one of the advantages of geothermal energy compared with fossil fuels; another advantage is that it is environmentally more friendly [6–8]. The development and utilization of geothermal energy has grown in the last few decades. According to Finger and Blankenship [3], in 2005 the worldwide electricity production from geothermal energy was responsible for reducing the consumption of more than thirty million barrels of oil. As indicated by Lund [9], heat pumps using geothermal sources have ‘the largest energy use’ which can be utilized.

High concentration of geothermal energy is usually available in the deepest parts of the Earth. For example, in most of North America, in the regions to the east of the Rocky Mountains, the ground temperature is about 135 °C at depths of 5–7 km [3]. The main objective is to access the stored geothermal energy. Fluid flowing in the well during the drilling operation is called the drilling fluid or the drilling mud; it is generally considered to be a nonlinear complex fluid comprised of cuttings (solid particles) with various sizes and shapes suspended in a base fluid and is primarily used to

transport the particles/cuttings generated during the drilling process from the bottom hole to the surface [10,11]. Successful operation of drilling requires, among other things, a thorough understanding of the rheological and thermal properties of the drilling fluid, [11–13]; this has motivated numerous experimental and theoretical studies [12,14–16]. For example, heat transport in the drilling fluid and temperature control at the drill bit plays a major role in the success of enhanced geothermal system (EGS) technology, which is applied in deep subsurface areas where the temperature is in the range of 150–200 °C (see Rybach [17]).

In most cases, the drilling fluid is modeled using the Power law model, the Bingham model or the Herschel–Bulkley model (which combines the effects of the Bingham and the power-law models [18–20]). For the Herschel–Bulkley model, it is assumed that the material behaves like a solid when the (shear) stress is below the yield stress, and like a shear-thinning or shear thickening fluid when the (shear) stress exceeds the yield stress [21]. Moreover, the rheological properties of the drilling fluid can also depend on pressure, volume fraction of the particles, shear rate, temperature, etc. Krieger [22] performed experimental and theoretical studies to describe the relation between volume fraction, shear rate and shear viscosity of a suspension. Briscoe et al. [23] proposed a viscosity model for concentrated suspensions, which shows the dependency of viscosity on pressure and temperature. Their model is suitable for high pressure and high temperature conditions, such as deep ocean drilling. In addition, the thermal diffusivity of the drilling mud also shows nonlinear behavior and depends on the particle concentration, size and shape of the particles [16,24–27]. As indicated by Agemar et al. [28], the most important parameter when considering the thermal aspects of a geothermal reservoir is temperature and its variation.

In most cases, the drilling fluid is modeled using the Power law model, the Bingham model or the Herschel–Bulkley model (which combines the effects of the Bingham and the power-law models [18–20]). For the Herschel–Bulkley model, it is assumed that the material behaves like a solid when the (shear) stress is below the yield stress, and like a shear-thinning or shear thickening fluid when the (shear) stress exceeds the yield stress [21]. Moreover, the rheological properties of the drilling fluid can also depend on pressure, volume fraction of the particles, shear rate, temperature, etc. Krieger [22] performed experimental and theoretical studies to describe the relation between volume fraction, shear rate and shear viscosity of a suspension. Briscoe et al. [23] proposed a viscosity model for concentrated suspensions, which shows the dependency of viscosity on pressure and temperature. Their model is suitable for high pressure and high temperature conditions, such as deep ocean drilling. In addition, the thermal diffusivity of the drilling mud also shows nonlinear behavior and depends on the particle concentration, size and shape of the particles [16,24–27]. As indicated by Agemar et al. [28], the most important parameter when considering the thermal aspects of a geothermal reservoir is temperature and its variation.

Here, we model the drilling fluid as a suspension with nonlinear rheological properties, where the viscosity and the thermal conductivity depend on the volume fraction, shear rate, temperature etc., and the motion of the solid particles depends on the particles collision, non-uniform distribution of the viscosity [29] and turbulent diffusivity. It is worth mentioning that, in general, suspensions can also be modeled using multi-component approaches (see [30–32]). In Section 2, the governing conservation equations for mass, linear and angular momentum, solid concentration and energy are discussed. In Section 3, the constitutive equations for the stress tensor of the suspension, the non-linear diffusive particle flux, internal energy and the heat flux vector are provided. Then in Section 4, the governing equations are non-dimensionalized and two flow conditions are considered and numerically solved: flow in a pipe and flow between two eccentric cylinders where the inner cylinder is rotating. We study the effects of various conditions encountered in geothermal well drilling operations, such as the earth temperature, the rotational speed of the inner cylinder, and the bulk volume fraction of solid particles on the flow and heat transfer.

## 2. Governing Equations

In general, using the methods of continuum mechanics, a suspension can be mathematically studied using three different methods: (1) the single phase approach where the suspension is modeled as a single-component fluid; (2) the non-homogenous single phase model where the particle motion is studied using a particle concentration equation with proper nonlinear flux terms [29,33]; (3) the two-fluid (two-phase) approach, e.g., Mixture theory approach [31,34,35], where the fluid and solid components are coupled through interaction forces. In current work, the non-homogenous single phase model will be used; this approach retains several important features of the two-fluid (two-phase) approach, with lower computational cost [36]. If the effects of electro-magnetism and chemical reactions are ignored, the governing equations, for a single component suspension, are the conservation equations for mass, linear and angular momentum, particle concentration, and energy [11,33,36,37].

### 2.1. Conservation of Mass

The conservation equation of mass is,

$$\frac{\partial \rho_m}{\partial t} + \text{div}(\rho_m \mathbf{v}) = 0 \quad (1)$$

where  $\rho_m = (1 - \phi)\rho_{f0} + \phi\rho_{s0} = \alpha\rho_{f0} + \phi\rho_{s0}$  is the density of the suspension,  $\phi$  is the volume fraction of the particles,  $\rho_{f0}$  and  $\rho_{s0}$  are the pure density of fluid and solid components in the reference configuration, i.e., before mixing the suspension is formed, respectively;  $\mathbf{v}$  is the velocity vector and  $\partial/\partial t$  is the partial derivative with respect to time. For an isochoric motion:

$$\text{div} \mathbf{v} = 0 \quad (2)$$

### 2.2. Conservation of Linear Momentum

The conservation of linear momentum is,

$$\rho_m \frac{d\mathbf{v}}{dt} = \text{div} \mathbf{T} + \rho_m \mathbf{b} \quad (3)$$

where  $\mathbf{b}$  is the body force vector,  $\mathbf{T}$  is the Cauchy stress tensor, and  $d/dt$  is the total material time derivative, which is given by  $d(\cdot)/dt = \partial(\cdot)/\partial t + [\text{grad}(\cdot)]\mathbf{v}$ . The conservation of angular momentum indicates that in the absence of couple stresses the stress tensor is symmetric, that is,  $\mathbf{T} = \mathbf{T}^T$  [36].

### 2.3. Conservation of Volume Fraction (Convection-Diffusion Equation)

The conservation of volume fraction is,

$$\frac{\partial \phi}{\partial t} + \mathbf{v} \frac{\partial \phi}{\partial \mathbf{x}} = -\text{div} \mathbf{N} \quad (4)$$

where the first term on the left-hand side denotes the rate of accumulation of particles, the second term denotes the convected particle flux, and the term on the right-hand side denotes the diffusive particle flux [11]. Following Phillips et al. [29], the particle flux  $\mathbf{N}$  is assumed to be related to the Brownian motion (see [38,39] for additional details), the variation of interaction frequency and the viscosity.

### 2.4. Conservation of Energy

The conservation of energy reads,

$$\rho_m c_m \frac{d\theta}{dt} = \mathbf{T} : \mathbf{L} - \text{div} \mathbf{q} + \rho_m r \quad (5)$$

where  $\mathbf{q}$  is the heat flux vector,  $\mathbf{L}$  is the gradient of velocity, and  $r$  is the specific radiant energy.  $\rho_m c_m = (1 - \phi)\rho_{f0}c_{pf0} + \phi\rho_{s0}c_{ps0}$  is the heat capacity of the suspension and  $c_{pf0}$  and  $c_{ps0}$  are the specific heat capacity of the pure fluid and the solid particles in reference configuration. Thermodynamic requires the application of the second law of thermodynamics [40]. The local form of the entropy inequality is given by ([40]):

$$\rho_m \dot{\eta} + \text{div } \boldsymbol{\varphi} - \rho_m s \geq 0 \quad (6)$$

where  $\eta(\mathbf{x}, t)$  is the specific entropy density,  $\boldsymbol{\varphi}(\mathbf{x}, t)$  is the entropy flux, and  $s$  is the entropy supply density due to external sources, and the dot denotes the material time derivative [40]. If  $\boldsymbol{\varphi} = \frac{1}{\theta} \mathbf{q}$ , and  $s = \frac{1}{\theta} r$ , where  $\theta$  is the absolute temperature, then Equation (5) reduces to the more familiar Clausius-Duhem inequality

$$\rho_m \dot{\eta} + \text{div } \frac{\mathbf{q}}{\theta} - \rho_m \frac{r}{\theta} \geq 0 \quad (7)$$

The effects of the Clausius-Duhem inequality are ignored in this paper; we present the above equation for the sake of completeness [41–44]. In order to ‘close’ the above set of equations, constitutive relations are needed for  $\mathbf{T}$ ,  $\mathbf{q}$ , and  $\mathbf{N}$ . We ignore the effects of radiation.

### 3. Constitutive Equations

#### 3.1. Stress Tensor

In general, the constitutive equation for the stress tensor of a concentrated suspension can be given by a non-Newtonian (non-linear) model (see [22,45]) and it may include a viscous stress and a yield stress (see [11,12]):

$$\mathbf{T} = \mathbf{T}_y + \mathbf{T}_v \quad (8)$$

where  $\mathbf{T}_y$  and  $\mathbf{T}_v$  are the yield stress and the viscous stress, respectively. Here, we focus on the viscous stress and assume that the suspension can be modeled as a viscous fluid,

$$\mathbf{T} = -p\mathbf{I} + \mu_m \mathbf{D} \quad (9)$$

where  $\mu_m$  is the viscosity of the suspension,  $\mathbf{I}$  is the identity tensor,  $\mathbf{D}$  is the symmetric part of the velocity gradient, and  $p$  is the pressure [36]. In general, the shear viscosity can depend on,

$$\mu_m = \mu_m(t, \dot{\gamma}, \theta, \phi, p, \mathbf{E}, \mathbf{B}) \quad (10)$$

where  $t$  is the time,  $\dot{\gamma}$  is some measure of the shear rate,  $\theta$  the temperature,  $\phi$  the concentration,  $p$  the pressure,  $\mathbf{E}$  the electric field, and  $\mathbf{B}$  the magnetic field [46]. In this paper, we will not consider the effects of time, electric or magnetic fields on the viscosity. We assume the viscous stress part of the suspension can be represented by a generalized power-law fluid model [22,23,33], where:

$$\mathbf{T}_v = -p\mathbf{I} + \left( \mu_t + \mu_r(p, \theta) \left( 1 - \frac{\phi}{\phi_{max}} \right)^{-\beta} \Pi^{\frac{m}{2}} \right) \mathbf{D} \quad (11)$$

$$\mu_r = \mu_{r0} e^{\frac{C_{10} p \theta E_u - C_{20} p}{k_B (\theta - \theta_c)}}; \mu_m = \mu_r \left( 1 - \frac{\phi}{\phi_{max}} \right)^{-\beta} \Pi^{\frac{m}{2}} \quad (12)$$

$$\Pi = 2tr\mathbf{D}^2, \mathbf{D} = \frac{1}{2}(\mathbf{L} + \mathbf{L}^T), \mathbf{L} = \text{grad } \mathbf{v} \quad (13)$$

Here  $\mu_t$  is the turbulence eddy viscosity,  $\theta$  is temperature,  $tr$  is the trace operator,  $\Pi$  is an invariant of  $\mathbf{D}$ ,  $E_u$  is related to the ‘‘activation energy’’,  $k_B$  is the Boltzmann constant,  $C_{10}$ ,  $C_{20}$  and  $\theta_c$  are constants related to temperature effects, and  $m$  is a measure of the shear dependency of the viscosity.

The expression,  $\mu_{r0}(1 - \frac{\phi}{\phi_{max}})^{-\beta}$  is based on Krieger's work who provided a correlation for the viscosity of the suspension as a function of the particle concentration ( $\mu = \mu_{f0}(1 - \phi/0.68)^{-1.82}$ ) [22]; this paper included theoretical analysis and experimental studies using various sizes and types of particles,  $\phi_{max}$  is the volume fraction of the particles under the maximum packing condition.  $\mu_r$  in Equation (12) is a generalization of the model proposed by Briscoe (1994) [23]. In the remainder of this study, we ignore the shear rate dependency of the viscosity. However, for suspensions with smaller size particles (such as nanofluids), the effect of the shear rate on viscosity can be significant [46,47]. The parameters in the expression for  $\mu_r$  depend on the properties of the specific drilling mud which need to be determined using experiments. Here we use the data used in the experiments performed by Wang et al. [16]; the values of the following parameters are fitted to their data:  $\mu_{r0} = 0.4153$  cp,  $C_1 = \frac{C_{10}pE_u}{k_B} = 2.3981$ ,  $C_2 = \frac{C_{20}p}{k_B} = 46.3226$  K and  $\theta_c = 182.3742$  K. In these measurements, the shear rate ranged from 0 to  $1020 \text{ s}^{-1}$ ; the shear viscosity was found to be independent of the shear rate, see Wang et al. [16]. The bulk volume fraction is 0.345. The drilling mud is composed of water, various additives and solid particles. The density of the drilling mud is  $2.2 \text{ g/cm}^3$ . Comparison between the fitted expression and the experimental data are shown in Figure 1. We should mention that there are other models for drilling fluids for high pressure and high temperature (HPHT) conditions. Most of these models are based on the Herschel-Bulkley model (see Khan and May [48], Salehi et al. [49], Vajargah and van Oort [50]). Our model not only includes the effects of temperature and shear-rate dependency of the viscosity, but also allows for a volume fraction dependent viscosity and thermal conductivity. Next we discuss the modeling of the particle flux  $N$ .

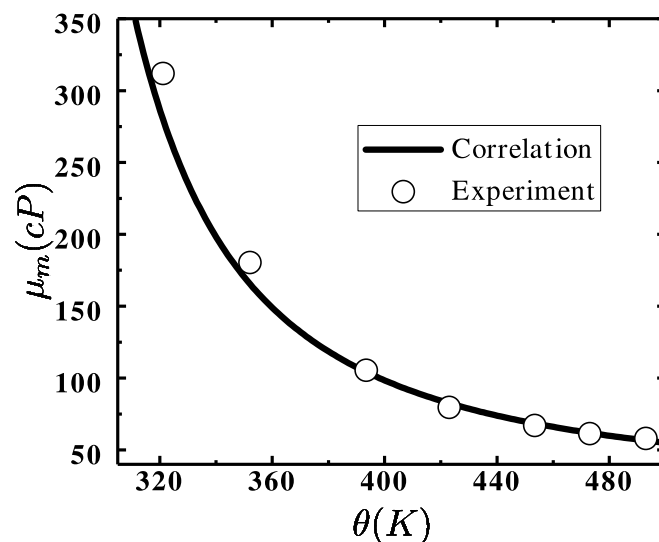


**Figure 1.** Dependency of the suspension viscosity on the temperature. The bulk volume fraction is 0.345 and the density of the drilling mud is  $2.2 \text{ g/cm}^3$ . Experimental data is from Wang et al. [16].

### 3.2. Particle Flux

The particle transport flux (the volume fraction equation) can be due to sedimentation, turbulent diffusivity, Brownian motion, etc. [13,29]. In this study, we ignore the Brownian motion. Thus, the diffusive particle flux can be written as:

$$N = N_c + N_\mu + N_g + N_t \quad (14)$$

where  $N_c$ ,  $N_\mu$ ,  $N_g$  and  $N_t$  are the contributions due to particles collision, spatial variations in the viscosity, gravity and turbulence, respectively. In this paper, we also assume  $N_g = \mathbf{0}$ . Based on the proposal of Phillips et al. [29], we assume  $N_c$  and  $N_\mu$  are given by:

$$N_c = -a^2 \phi K_c \nabla(\dot{\gamma} \phi) \quad (15)$$

$$N_\mu = -a^2 \phi^2 \dot{\gamma} K_\mu \nabla(\ln \mu_s) \quad (16)$$

$$\dot{\gamma} = (2\mathbf{D}_{ij} \mathbf{D}_{ij})^{1/2} = (\Pi)^2 \quad (17)$$

where  $a$  is the radius of the particle,  $\dot{\gamma}$  is the local shear rate,  $\mu_s$  is the effective viscosity, and  $K_c$ ,  $K_\mu$  are empirically-determined coefficients. According to Seifu et al. [51] the above two terms in the particle flux are given by,

$$N_c + N_\mu = -a^2 K_c \phi^2 \dot{\gamma} \nabla(\ln(\dot{\gamma} \phi \mu_s^{K_\mu/K_c})) \quad (18)$$

We can see that  $\ln(\dot{\gamma} \phi \mu_s^{K_\mu/K_c})$  is a field potential incorporating mechanism which can cause migration of the particles. Following the Phillips et al. and Subia et al. [13,29], in this paper we assumed that  $K_c = 0.43$ ,  $K_\mu = 0.62$ , as constants.

The turbulent diffusivity flux is given by [52],

$$N_t = -\frac{v_t}{Sc} \nabla(\phi) \quad (19)$$

where  $v_t$  is the eddy diffusivity and  $Sc$  is the Schmidt number assumed to be 0.9 for the present study [53,54].

### 3.3. Heat Flux Vector

As stated by Fourier [55] (see also Winterton [56]), the heat flux vector is proportional to the gradient of temperature,

$$\mathbf{q} = -k \nabla \theta \quad (20)$$

where  $k$  is the thermal conductivity of the material [36]. For complex materials,  $k$  can depend on various parameters/fields, such as concentration, temperature, shear rate, etc.; in these situations  $k$  is usually replaced with  $k_m$  or  $k_{eff}$ , called the effective thermal conductivity. In general,  $k$  is a second order tensor for anisotropic materials (for more information see [57], p. 129 and [58–60]). When turbulence is considered, there is an additional contribution to the conduction usually designated as  $k_t$  [61,62],

$$k = k_m + k_t = k_m + \frac{v_t}{Pr_t} \rho_f \quad (21)$$

where  $Pr_t$  is the Prandtl number and can be chosen as 8/9 [61]. An effective thermal conductivity model derived by Jeffrey [26] is:

$$k_m = \kappa_f [1 + 3\tilde{\xi} \phi + \hat{\xi} \phi^2] + O(\phi^3) \quad (22)$$

where:

$$\hat{\xi} = 3\tilde{\xi}^2 + \frac{3\tilde{\xi}^3}{4} + \frac{9\tilde{\xi}^3}{16} \left( \frac{\omega + 2}{2\omega + 3} \right) + \frac{3\tilde{\xi}^4}{26} + \dots \quad (23)$$

where:

$$\tilde{\xi} = \frac{\omega - 1}{\omega + 2} \quad (24)$$

Jeffrey's model includes second order effects in the volume fraction, see also [63]. It is worth mentioning that Equation (22) is a (corrected) linearization of the Maxwell formula, which can be rewritten as,

$$k_m = \kappa_f \frac{1 + 2\xi\phi}{1 - \xi\phi} \quad (25)$$

For more information about the effective heat conductivity of suspensions, see [64]. In our paper here, we use the model proposed by Jeffrey [26]. The heat conductivity of the suspending fluid (water),  $\kappa_f$ , is assumed to be 0.6485 W/(m·K) [65].

In the following section, we present the three-dimensional forms of the governing equations. After non-dimensionalizing these equations, we study two different problems (1) flow in a long vertical pipe; and (2) flow between two eccentric rotating cylinders. For each geometry, we first study problems with isothermal condition, and then we look at the effect of the temperature, namely problems with non-uniform temperature distribution.

#### 4. Results and Discussion

Substituting Equations (13)–(14), (14)–(19) and (20)–(24) in Equations (1)–(5), a set of partial differential equations (PDEs) are obtained. The PDEs are given below:

$$\text{div}(\mathbf{v}) = 0 \quad (26)$$

$$\rho_m \left( \frac{\partial \mathbf{v}}{\partial t} + (\text{grad } \mathbf{v}) \mathbf{v} \right) = -\text{grad } p + \text{div} \left( (\mu_t + \mu_m) \mathbf{D} \right) \quad (27)$$

$$\frac{\partial \phi}{\partial t} + \mathbf{v} \frac{\partial \phi}{\partial x} = \text{div} (a^2 \phi K_c \dot{\gamma} \nabla(\phi)) + \text{div} (a^2 \phi K_c (\dot{\gamma}) \nabla \phi + a^2 \dot{\gamma} K_\mu \nabla (\ln \mu_m) \phi^2) + \text{div} \left( \frac{v_t}{Sc} \nabla(\phi) \right) \quad (28)$$

$$\begin{aligned} & \left( (1 - \phi) \rho_{f0} C_{pf0} + \phi \rho_{s0} C_{ps0} \right) \left( \frac{\partial \theta}{\partial t} + (\text{grad } \theta) \mathbf{v} \right) \\ & = ((\mu_t + \mu_m) \mathbf{D}) : \mathbf{L} + \text{div} \left( \left( \frac{v_t \rho_f}{Pr_t} + \kappa_f (1 + 3\xi\phi + \xi\phi^2) \right) \nabla \theta \right) \end{aligned} \quad (29)$$

The above equations are used to solve for the unknowns which are,  $\mathbf{v}$ ,  $p$ ,  $\phi$  and  $\theta$ . The dimensionless forms of the above equations are,

$$\text{div}(\mathbf{V}) = 0 \quad (30)$$

$$\rho_m \left( \frac{\partial \mathbf{V}}{\partial \tau} + (\text{grad } \mathbf{V}) \mathbf{V} \right) = -\text{grad } P + \frac{1}{Re} \text{div} \left( \frac{(\mu_t + \mu_m)}{\mu_r} \mathbf{D} \right) \quad (31)$$

$$\frac{\partial \phi}{\partial \tau} + \mathbf{V} \text{grad } \phi = \text{div} (J_c \Gamma \phi \nabla(\phi)) + \text{div} \left( J_c \nabla(\Gamma) \phi^2 + J_\mu \Gamma \frac{\nabla(\mu_m)}{\mu_m} \phi^2 \right) + \text{div} \left( \frac{v_t}{ScHu_0} \nabla(\phi) \right) \quad (32)$$

$$\begin{aligned} & (\alpha \rho_{f0} C_{pf0} + \phi \rho_{s0} C_{ps0}) \left( \frac{\partial \bar{\theta}}{\partial \tau} + (\text{grad } \bar{\theta}) \mathbf{V} \right) \\ & = R \left( \frac{(\mu_t + \mu_m)}{\mu_r} \mathbf{D} \right) : \mathbf{L} + \frac{1}{RePr} \text{div} \left( \frac{\kappa_t + \kappa_m}{\kappa_f} \nabla \bar{\theta} \right) \end{aligned} \quad (33)$$

where:

$$Y = \frac{y}{H_r}; X = \frac{x}{H_r}; Z = \frac{z}{H_r}; \mathbf{V} = \frac{\mathbf{v}}{u_0}; \tau = \frac{tu_0}{H_r}; \bar{\theta} = \frac{\theta - \theta_0}{\theta_1 - \theta_0}; \Gamma = \frac{H_r \dot{\gamma}}{u_0};$$

$$\rho_m^* = \frac{\rho_m}{\rho_{f0}}; \rho_{f0}^* = \frac{\rho_{f0}}{\rho_{f0}}; \rho_{s0}^* = \frac{\rho_{s0}}{\rho_{f0}}; C_{pf0}^* = \frac{C_{pf0}}{C_{pf0}}; C_{ps0}^* = \frac{C_{ps0}}{C_{pf0}};$$

$$\text{div}^*(\cdot) = H_r \text{div}(\cdot); \text{grad}^*(\cdot) = H_r \text{grad}(\cdot);$$

$$\mathbf{L}^* = \text{grad}^* \mathbf{V}; \mathbf{D}^* = \frac{1}{2} [\text{grad}^* \mathbf{V} + (\text{grad}^* \mathbf{V})^T];$$

$$P^* = \frac{p}{\rho_{f0}u_0^2}; Re = \frac{\rho_{f0}u_0H_r}{\mu_r}; J_c = \frac{a^2K_c}{H_r^2}; J_\mu = \frac{a^2K_\mu}{H_r^2};$$

$$D_s = \frac{\mu_r u_0}{H_r \rho_{f0} C_{pf0} (\theta_1 - \theta_0)}; Pr = \frac{C_{pf0} \mu_r}{k_f};$$

where  $H_r$  is a reference length, for example, the diameter of the pipe,  $u_0$  is a reference velocity and is chosen as the axial mean velocity at the inlet, and  $\theta_1$  and  $\theta_0$  are reference temperatures and are chosen as 393 K and 293 K, respectively. The asterisks have been dropped for simplicity. Among the above dimensionless numbers  $J_c$  and  $J_\mu$  are related to the particles flux;  $D_s$  is related to the heat dissipation. For obtaining the turbulent eddy diffusivity  $\nu_t$  (and the turbulent eddy viscosity  $\mu_t$ ), different turbulence models, such as  $k - \omega$  or  $k - \epsilon$  RANS model, can be selected depending on the flow conditions [66–68]. In this paper, we also ignore the effect of the turbulence, due to the low Reynolds number of the problems studied. Table 1 lists the value of the physical properties applied in this paper. The suspension viscosity, effective thermal conductivity and  $K_c$  are calculated by the models/correlations discussed in the previous section.

Numerically, the above governing equations are solved by developing PDE solver using the libraries of OpenFOAM® [69]. The PIMPLE algorithm is applied for dealing with the incompressibility condition [69]. The details of how the governing equations are discretized in OpenFOAM, the PIMPLE algorithm, the numerical schemes, etc., are given on [69–73]. For ensuring numerical stability and accuracy, the value of the time step is chosen so that the maximum Courant Number is always less than 0.1. The Courant Number is the portion of a cell that a material will transport by advection in one time step. The boundary conditions are provided in Table 2, for more detail see [71]. For each problem, the simulation domain is discretized as hexahedral meshes using ICEM [74]. The mesh-dependence studies are performed for each case.

In the following cases studied, we assume  $D_s = 0$ , that is we ignore the effect of viscous dissipation; and due to the low Reynolds number of the problems we also ignore the effect of the turbulence on flow, heat transfer and particles transport.

**Table 1.** Physical properties used in this paper [29,65,75,76].

Physical Property	Value	Physical Property	Value
$\rho_{f0}$	1000 kg/m <sup>3</sup>	$c_{pf0}$	4020 J/(kg·K)
$\rho_{s0}$	4480 kg/m <sup>3</sup>	$c_{ps0}$	460 J/(kg·K)
$a$	1.25 mm	$\kappa_f$	0.6485 W/(m·K)
$K_\mu$	0.62	$\omega$	2.0

**Table 2.** Boundary conditions. For more discussion on the boundary condition, see [71].

Boundary	Pressure	Velocity	Volume Fraction	Temperature
Wall	Fixed flux (0)	Fixed value	Fixed flux (0)	Fixed value
Inlet	Fixed value (0)	Fixed value	Fixed value (0)	Fixed value
Outlet	Fixed value (0)	Fixed flux (0)	Fixed flux (0)	Fixed flux (0)

#### 4.1. Vertical Flow in a Pipe

First, we study the flow in a vertical pipe, as shown in Figure 2. The pipe is assumed to be embedded in earth. To save computational cost while simulating the flow in a long pipe, we use the symmetry condition and assume that the flow is two dimensional. Furthermore, to ensure a steady-state condition, the simulation time is always set to be greater than  $5 \cdot (L/U)$ , where  $L$  is the length of the pipe and  $U$  is the mean velocity of the flow.

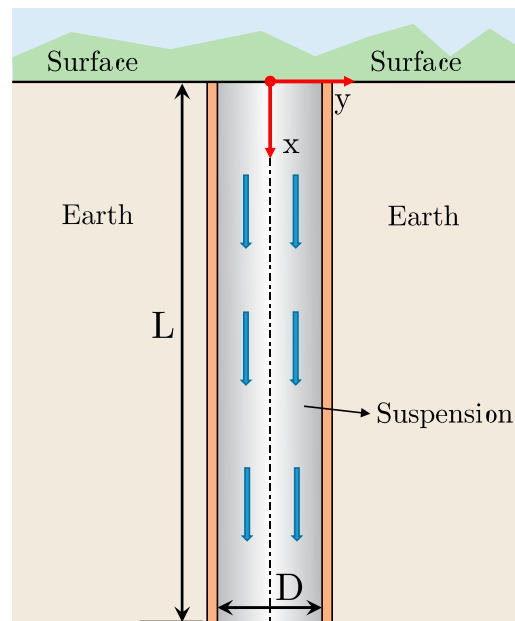


Figure 2. Schematic of the pipe.

#### 4.1.1. Effect of Bulk Volume Fraction and the Reynolds Number

From Equation (11) we can see that the concentration of the solid particles affects the viscosity of the suspension, especially when the volume fraction is close to the maximum packing volume fraction. We assume isothermal conditions, i.e.,  $\bar{\theta}$  is zero. Based on the flow conditions at the inlet, the values of the dimensionless numbers are:  $Re = 159$ ,  $J_{\mu} = 3.87 \times 10^{-4}$  and  $Pr = 971$ . Here the characteristic length  $H_r$  is chosen as the diameter of the pipe,  $D$ . The length of the pipe is  $L = 100D$ , for ensuring that the flow is fully developed.

Figure 3a shows the relative volume fraction profiles, defined as  $\phi/\bar{\phi}$ , for different values of the bulk solid volume fraction,  $\bar{\phi}$ . The volume fraction distribution is more uniform when  $\bar{\phi}$  is large. In our model, when the flow is isothermal the non-uniform distribution of particles is mainly attributed to the collision rate of the particles (related to the shear rate), corresponding to the term  $N_c$  in Equation (15). We expect that if the  $\bar{\phi}$  approaches the maximum packing value, the volume fraction distribution will almost be constant. At the same time, for higher values of  $\bar{\phi}$ , the concentration is more uniform near the pipe center. Figure 3b shows the velocity distributions with different values of  $\bar{\phi}$ . The velocity profiles become blunter as  $\bar{\phi}$  increases, perhaps due to the higher concentration near the center of the pipe.

In drilling applications, fresh water is pumped into the well to remove the solid cuttings. The cost of the pumping power, is related to the pressure drop. Figure 3c shows the pressure drop between the pipe inlet and the outlet for different values of  $\bar{\phi}$ . As  $\bar{\phi}$  increases, the pressure drop increases almost exponentially. Therefore, it is important to control or monitor the values of  $\bar{\phi}$  in order to have a more efficient drilling process; this can be accomplished by increasing the flow rate of freshly pumped water or by decreasing the rate of the penetration (ROP), where ROP is defined as the speed at which a drill bit breaks the rock to deepen the borehole [77]. The effect of the Reynolds number is negligible and will not be studied here [12,29].

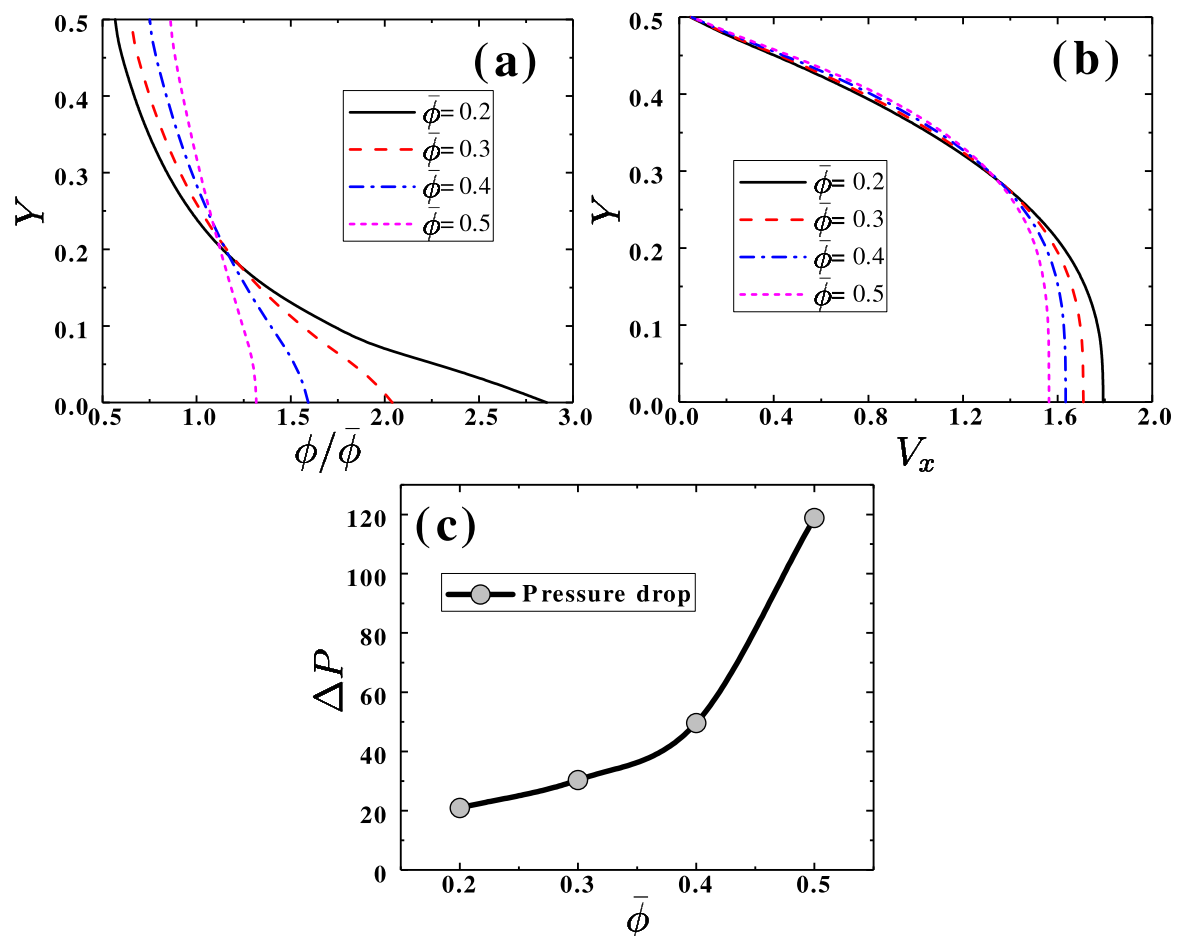


**Figure 3.** (a) The relative volume fraction profiles along the radial direction ( $Y$  direction as shown in Figure 2.) for different values of the bulk volume fraction,  $\bar{\phi}$ ; (b) The profiles of the axial ( $X$ -direction) velocity,  $V_x$ , along the radial direction; (c) pressure drop between the inlet and the outlet for different values of the bulk volume fraction  $\bar{\phi}$ .  $Re = 159$ ,  $J_\mu = 3.87 \times 10^{-4}$  and  $Pr = 971$ .

#### 4.1.2. Effect of Temperature in the Axial Direction

It is known the temperature of the Earth rises about  $2.5^\circ\text{C}$  per 100 meters of depth [3], although in some situations this may vary depending on the geographical location. Therefore, the effects of the earth temperature variation along the axial (vertical) direction need to be studied. Mathematically the change in the earth temperature can be represented as a variable temperature boundary condition on the outside wall of the pipe. It is a computationally intensive calculation if we are to simulate a practical pipe with length of several kilometers. Therefore, here we perform the simulations for a pipe with length of  $1200D$ , with a large temperature gradient along the axial direction; specifically, we assume  $0.05^\circ\text{C}$  per  $H_r$  increases.  $\bar{\theta}$  at the inlet is assumed to be zero. We also assume that the value of the bulk volume fraction is 0.2. The values of the dimensionless numbers for this case are based on the inlet conditions:  $Re = 159$ ,  $J_\mu = 3.86 \times 10^{-4}$  and  $Pr = 971$ .

Figure 4a shows the radial ( $Y$ -direction, see Figure 2) temperature distribution at different depths. Near the walls the temperature gradient is large; overall, the temperature increases as the  $Y$ -position gets closer to the hot wall, while near the center, the temperature is the same as the inlet temperature ( $\bar{\theta} = 0$ ). Figure 4b shows that as the depth (in the axial direction) increases, that is, as the wall temperature increases, the volume fraction turns out to be more non-uniform and more particles move toward the channel wall. This can be attributed to the decreasing of the viscosity near the hot wall. From the particle transport model, namely Equations (14)–(16), we can see that  $N_\mu$  causes the particles

to move from higher viscosity regions to regions with lower viscosity. This is perhaps the reason for the volume fraction near the wall being higher at larger depths. Similar to Figure 3b, Figure 4c shows that the velocity profiles are not affected much. Another important parameter is the pressure distribution in the axial direction. As the depth increases, the pressure gradient decreases a little, perhaps due to the decrease of the suspension viscosity, see Figure 4d.

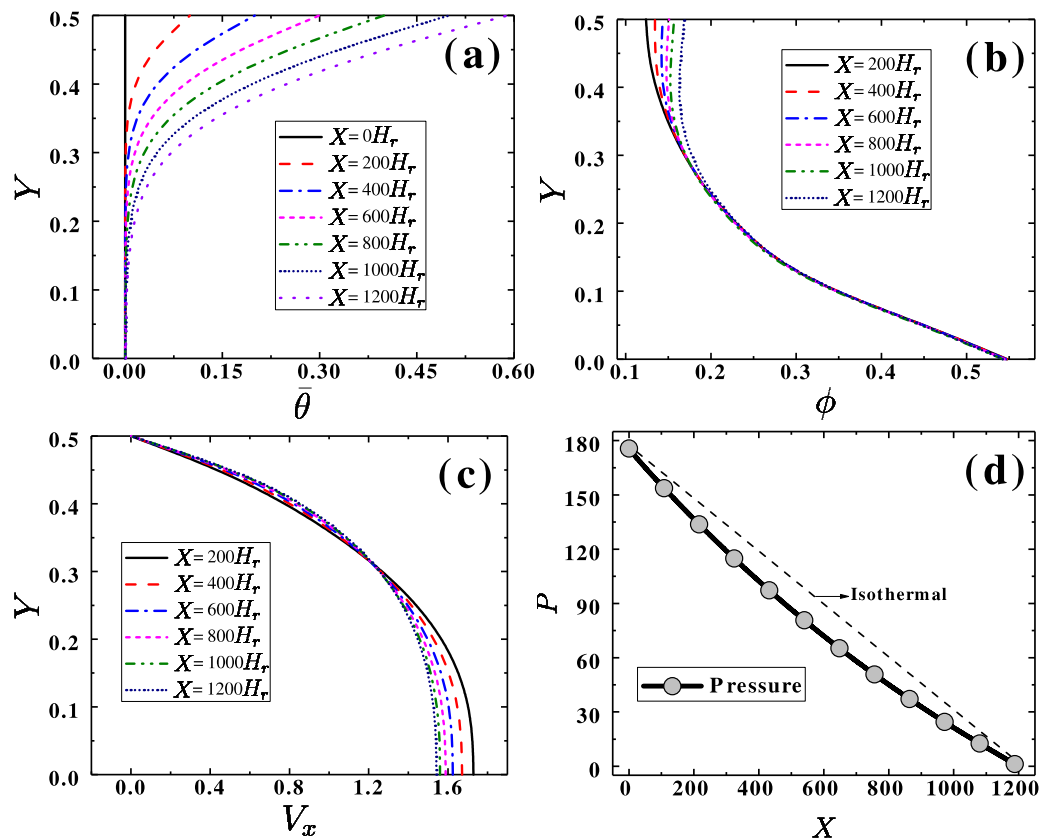


**Figure 4.** (a) Temperature distribution; (b) volume fraction; and (c) the velocity at different axial positions with the wall temperature (surrounding earth temperature) varying along the axial ( $X$ ) direction; (d) the pressure distribution at different axial positions with the wall temperature varying along the axial direction. The bulk volume fraction is 0.2, inlet  $\bar{\theta}$  is 0,  $Re = 159$ ,  $J_\mu = 3.86 \times 10^{-4}$  and  $Pr = 971$ .

#### 4.2. Flow between Two Eccentric Vertical Cylinders

In geothermal applications, the flow of the drilling suspension is usually represented by the simple geometry of the flow between two vertical cylinders with the inner cylinder rotating [78]. Figure 5 shows the geometry where the radius of the outer cylinder is 2.5 times of the radius of the inner cylinder;  $\varepsilon = e/(R_o - R_i) = 0.5$  is the eccentricity ratio, where  $e$  is the distance between the centers of the two cylinders. Here the hydraulic diameter of the channel,  $2(R_o - R_i)$ , is chosen as the characteristic length,  $H_r$ . The length of the cylinders is assumed to be  $100H_r$ , and the bulk volume fraction is 0.1. All the figures in the remainder of this paper are plotted along the line A-A as shown in Figure 5.

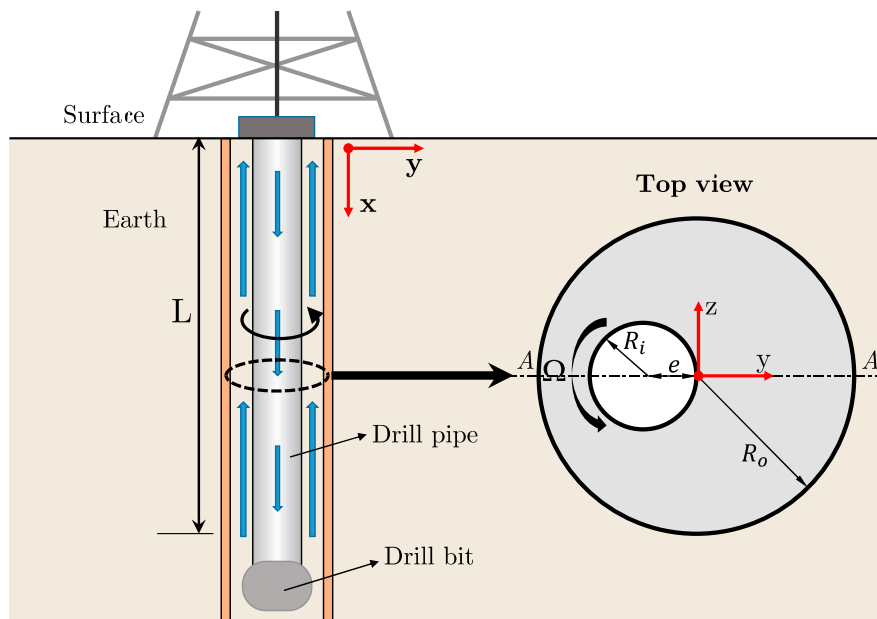


**Figure 5.** Geometry of the two eccentric cylinders. We assume  $L$  is the length of the simulated portion of the pipe, which is  $100H_r = 200(R_o - R_i)$ . The radius of the outer cylinder is 2.5 times of the inner, namely  $R_o = 2.5R_i$ . The eccentricity ratio is  $\varepsilon = e/(R_o - R_i) = 0.5$ .  $e$  is the distance between the center of the two cylinders.

#### 4.2.1. Effect of $Re_r$ (Rotational Speed)

An important parameter in drilling applications is the rotational speed of the inner cylinder. This determines the rate of penetration (ROP) [77], responsible for the amount of the solid cuttings produced, which in our problems is the bulk volume fraction. Clearly, the rotational speed,  $\Omega$ , also affects the flow field. For the current problem, we assume isothermal conditions, i.e.,  $\bar{\theta}$  is zero. Based on the inlet conditions, the values of the dimensionless numbers are:  $Re = 191.50$ ,  $J_\mu = 2.69 \times 10^{-4}$  and  $Pr = 971$ . For this flow situation, we define the Reynolds number as,  $Re_r = \rho_{f0}H_r(\Omega R_i)/\mu_r$ , which is related to the rotational speed of the inner cylinder. The values of  $Re_r$  are 0 ( $\Omega = 0$  RPM), 24.05 ( $\Omega = 60$  RPM) and 72.16 ( $\Omega = 180$  RPM).

Figure 6 shows the streamlines for different values of  $Re_r$ . As  $Re_r$  increases, the streamlines become more distorted. Figure 7 shows the volume fraction fields at the Z-Y plane at different axial positions (X coordinate) for different values of  $Re_r$ . For the cases shown in Figure 7 the flow is steady-state. With no rotation, the volume fraction distribution is symmetric along the A-A plane. The particles tend to accumulate near the center line, also see Figure 8a; this agrees with the results predicted by the multicomponent model of [79,80]. As  $Re_r$  increases, the particles tend to migrate in the direction of the angular speed of the inner cylinder; furthermore, we also notice that the high concentration of the solid particles in the narrow gap gradually begins to become more uniform, see Figure 8a as well. Figure 8b shows that except the region near the rotating cylinder, the change in the magnitude of the velocity profiles is moderate for different values of  $Re_r$ .

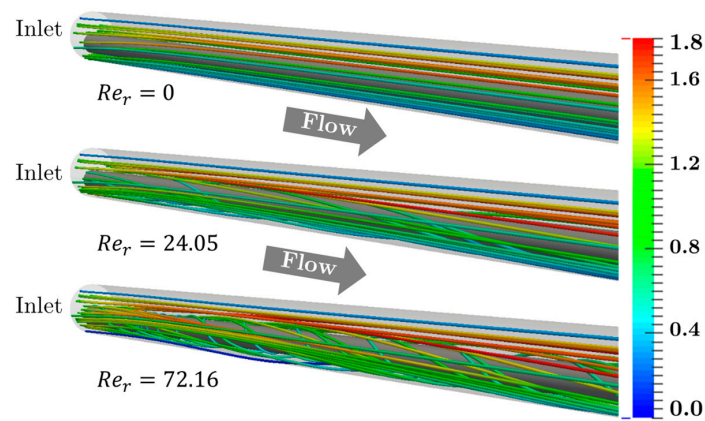


**Figure 6.** Streamlines for the isothermal flow between the two eccentric cylinders with different values of  $Re_r$  (related to the rotational speed).

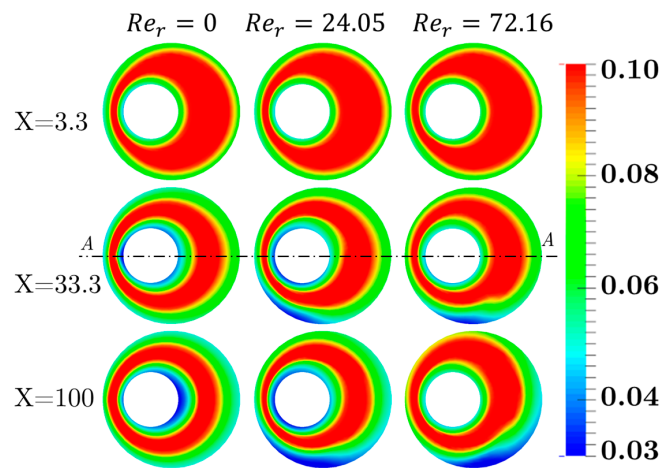


**Figure 7.** Top view. The volume fraction fields in the Z-Y plane for different dimensionless axial positions (X-direction) for different  $Re_r$  (rotational speed). The rotation is counter clockwise.

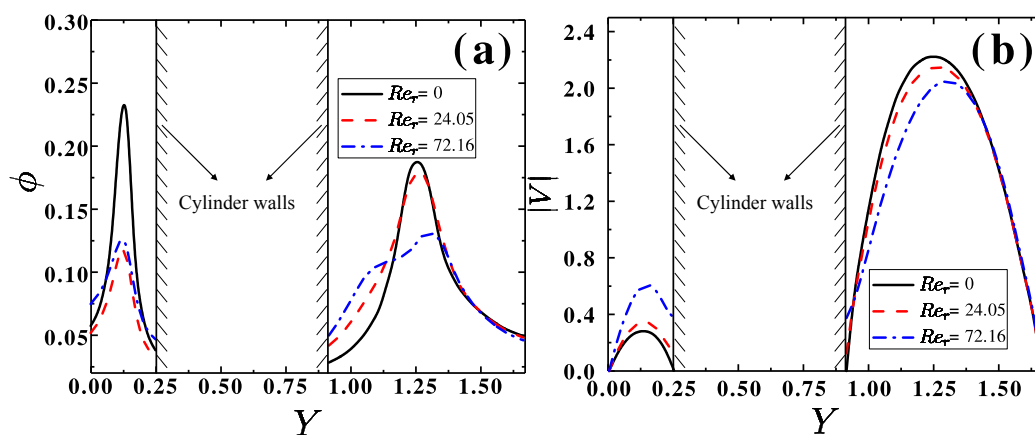


**Figure 8.** (a) The volume fraction and (b) the velocity profiles along the A-A plane (see Figure 5 also) near the outlet for different  $Re_r$ .

#### 4.2.2. Effects of the Earth Temperature

The wall temperature (or the outer cylinder) is assumed to be the same as the Earth temperature surrounding the cylinders. The value of  $\bar{\theta}$  at the inlet and at the wall of the inner cylinder is kept constant as zero, and  $Re_r = 36.08$  ( $\Omega = 90$  RPM). Based on the inlet conditions, the values of the dimensionless numbers for these simulations are:  $Re = 191.50$ ,  $J_\mu = 2.69 \times 10^{-4}$  and  $Pr = 971$ .

Figure 9 shows the profiles for the particles concentration, the temperature and the temperature gradient in the Z-Y plane at different axial positions and for different values of the outer wall temperature. By comparing Figure 9a with Figure 7, we notice that when the Earth (the surrounding) temperature is high, a thin layer of high particle concentration near the outer wall of the cylinder is formed (also see Figure 10a); this layer may be due to the non-uniform distribution of the suspension viscosity caused by the large temperature variation. This thin layer with a particle solid concentration may further enhance particles deposition near the outer cylinder. From Figure 9b, we can see that heat transfers from the outer cylinder to the interior of the flow occurs gradually; near the the outer cylinder the temperature gradient is much larger than the interior regions of the flow, also see Figure 10c; in addition, in the wide gap region, we can observe high temperatures which could be attributed to the convection caused by the rotation of the inner cylinder. Figures 9c and 10d indicate that the temperature gradient in the narrow gap is higher than the wide gap, which could be attributed to the stronger convective heat transfer in the narrow gap due to the inner cylinder rotation. The heat loss in the radial direction through the inner cylinder is not so clearly obvious; this can perhaps be attributed to the relatively high convective heat transfer along the axial direction. Figure 10d shows the velocity profiles for different values of the outer wall temperatures. As the wall temperature increases, in the wide gap region the location of the maximum velocity moves towards the outer cylinder.

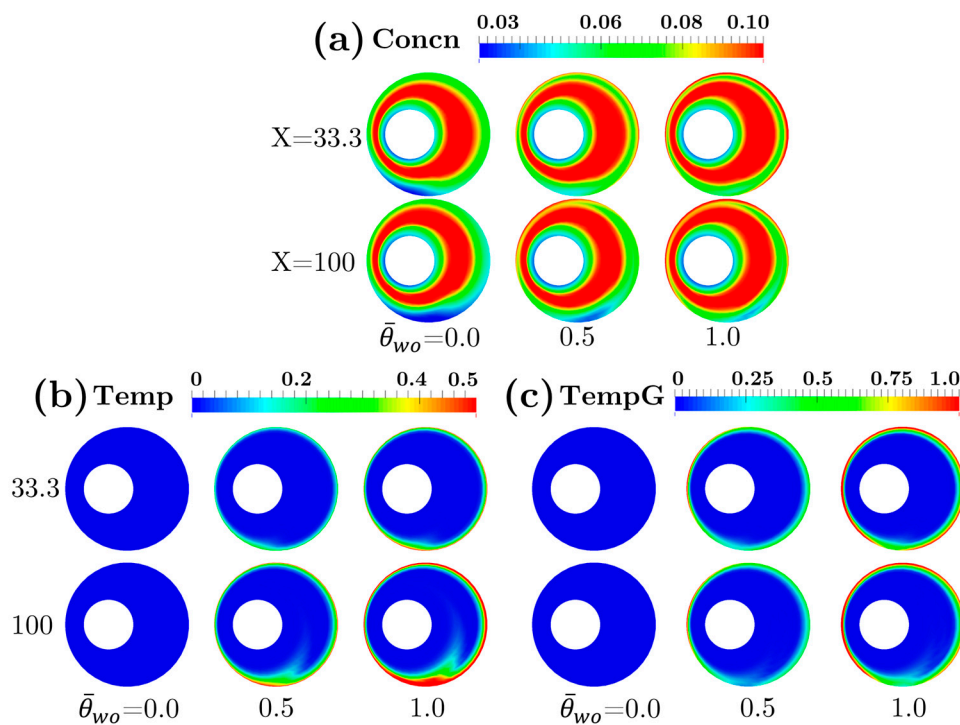


**Figure 9.** Top view. (a) The volume fraction and (b) the temperature (c) the temperature gradient fields in the Z-Y plane at different axial positions and different outer-wall temperatures, when  $Re_r = 36.8$  ( $\Omega = 90$  RPM), and  $\bar{\theta}$  at the inlet and at the inner cylinder wall is 0. The unit of the scale bar for the temperature gradient is  $10^4$ .

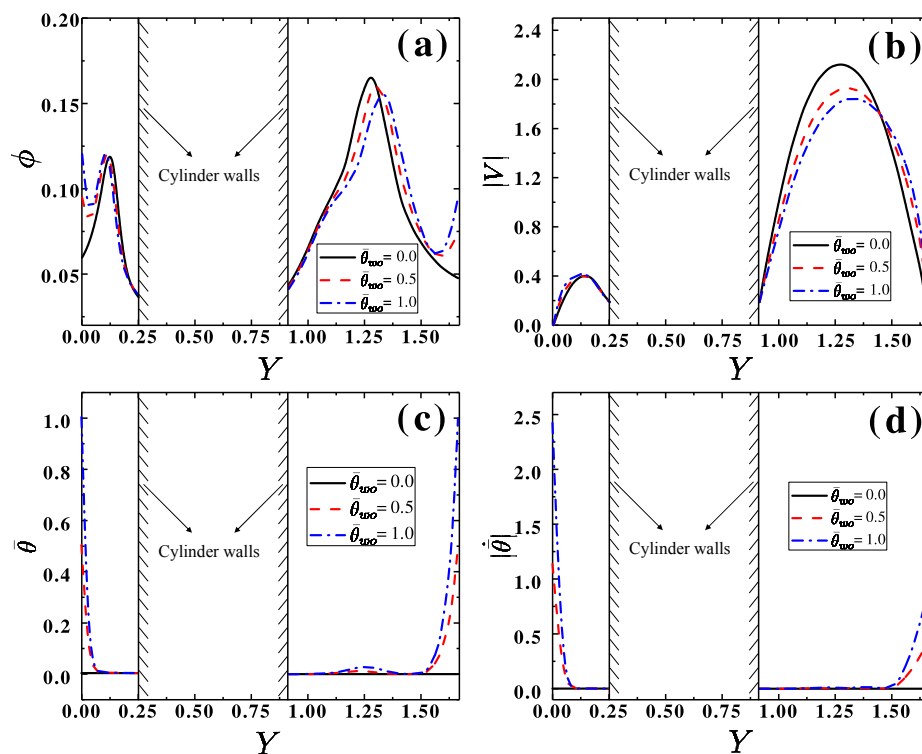


**Figure 10.** (a) The volume fraction profiles; (b) the velocity profiles; (c) the temperature profiles and (d) the temperature gradient profiles for different values of the earth temperature (wall temperature of the outer cylinder), when  $Re_r = 36.8$  ( $\Omega = 90$  RPM) and  $\bar{\theta}$  at the inlet and the inner cylinder wall is 0.

## 5. Concluding Remarks

In this study, we look at the heat transfer in a drilling fluid. The fluid is assumed to be a suspension composed of various components with complex rheological behavior. We model this suspension as a non-linear fluid, where the viscosity and the heat diffusivity depend on the concentration of the particle, the shear rate and temperature. The motion of the particles is based on a particle flux equation, where a generalization of the model proposed by [29] is used. By performing numerical studies for two different flow conditions, namely the flow in a vertical pipe and flow between two rotating cylinders with various boundary and flow conditions, we observe that the temperature and the flow fields depend significantly on the earth (surrounding) temperature distribution, the bulk volume fraction, etc. We also notice that for a large value of the (dimensionless) earth temperature, such as  $\bar{\theta}_{wo} = 1.0$ , a thin layer with high particle concentration is formed near the outer cylinder, which may enhance particle deposition in that region. Furthermore, as the bulk volume fraction increases, the pressure drop increases exponentially, perhaps due to the increase in the suspension viscosity. Finally, in certain applications, especially those involving gas-particle flows, such as fluidized bed reactors, under certain conditions, there could be a counter flow situations due to high solid loading (see Bednarz, et al. [81], Das et al. [82], Garić-Grulović et al. [83]). We did not consider this phenomenon in this paper.

**Author Contributions:** Wei-Tao Wu developed the framework of the paper and did the numerical simulations. Mehrdad Massoudi and Wei-Tao Wu derived the equations. Wei-Tao Wu, Nadine Aubry, James F. Antaki, Mark L. McKoy, and Mehrdad Massoudi prepared the manuscript.

**Conflicts of Interest:** The authors declare no conflict of interest.

## References

1. Younger, P.L. Geothermal energy: Delivering on the global potential. *Energies* **2015**, *8*, 11737–11754. [[CrossRef](#)]

2. Coussot, P. *Rheophysics*; Springer International Publishing: Cham, Switzerland, 2014.
3. Finger, J.; Blankenship, D. *Handbook of Best Practices for Geothermal Drilling*; Sandia National Laboratories: Albuquerque, NM, USA, 2010.
4. Sáez Blázquez, C.; Farfán Martín, A.; Martín Nieto, I.; Carrasco García, P.; Sánchez Pérez, L.; González-Aguilera, D. Efficiency Analysis of the Main Components of a Vertical Closed-Loop System in a Borehole Heat Exchanger. *Energies* **2017**, *10*, 201.
5. Congedo, P.M.; Lorusso, C.; De Giorgi, M.G.; Marti, R.; D'Agostino, D. Horizontal Air-Ground Heat Exchanger Performance and Humidity Simulation by Computational Fluid Dynamic Analysis. *Energies* **2016**, *9*, 930. [[CrossRef](#)]
6. Alhamid, M.I.; Daud, Y.; Surachman, A.; Sugiyono, A.; Aditya, H.B.; Mahlia, T.M.I. Potential of geothermal energy for electricity generation in Indonesia: A review. *Renew. Sustain. Energy Rev.* **2016**, *53*, 733–740.
7. Yavuzturk, C.; Spitler, J.D.; Rees, S.J. A transient two-dimensional finite volume model for the simulation of vertical U-tube ground heat exchangers. *ASHRAE Trans.* **1999**, *105*, 465–474.
8. He, M.; Rees, S.; Shao, L. Simulation of a domestic ground source heat pump system using a three-dimensional numerical borehole heat exchanger model. *J. Build. Perform. Simul.* **2011**, *4*, 141–155. [[CrossRef](#)]
9. Lund, J.W. Direct utilization of geothermal energy. *Energies* **2010**, *3*, 1443–1471. [[CrossRef](#)]
10. Rabia, H. *Oilwell Drilling Engineering: Principles and Practice*; Graham and Trotman Ltd.: London, UK, 1985.
11. Zhou, Z.; Wu, W.T.; Massoudi, M. Fully developed flow of a drilling fluid between two rotating cylinders. *Appl. Math. Comput.* **2016**, *281*, 266–277. [[CrossRef](#)]
12. Wu, W.T.; Massoudi, M. Heat Transfer and Dissipation Effects in the Flow of a Drilling Fluid. *Fluids* **2016**, *1*, 4. [[CrossRef](#)]
13. Subia, S.R.; Ingber, M.S.; Mondy, L.A.; Altobelli, S.A.; Graham, A.L. Modelling of concentrated suspensions using a continuum constitutive equation. *J. Fluid Mech.* **1998**, *373*, 193–219. [[CrossRef](#)]
14. Mahto, V.; Sharma, V.P. Rheological study of a water based oil well drilling fluid. *J. Pet. Sci. Eng.* **2004**, *45*, 123–128. [[CrossRef](#)]
15. Saasen, A.; Løklingholm, G. The effect of drilling fluid rheological properties on hole cleaning. In *IADC/SPE Drilling Conference*; Society of Petroleum Engineers: Dallas, TX, USA, 2002.
16. Wang, F.; Tan, X.; Wang, R.; Sun, M.; Wang, L.; Liu, J. High temperature and high pressure rheological properties of high-density water-based drilling fluids for deep wells. *Pet. Sci.* **2012**, *9*, 354–362. [[CrossRef](#)]
17. Rybach, L. Geothermal power growth 1995–2013—A comparison with other renewables. *Energies* **2014**, *7*, 4802–4812. [[CrossRef](#)]
18. Vajravelu, K.; Sreenadh, S.; Babu, V.R. Peristaltic transport of a Herschel–Bulkley fluid in an inclined tube. *Int. J. Non Linear Mech.* **2005**, *40*, 83–90. [[CrossRef](#)]
19. Herschel, W.H.; Bulkley, R. Konsistenzmessungen von gummi-benzollösungen. *Colloid Polym. Sci.* **1926**, *39*, 291–300. [[CrossRef](#)]
20. Papanastasiou, T.C. Flows of materials with yield. *J. Rheol.* **1987**, *31*, 385–404. [[CrossRef](#)]
21. Alexandrou, A.N.; McGilvray, T.M.; Burgos, G. Steady Herschel–Bulkley fluid flow in three-dimensional expansions. *J. Nonnewton. Fluid Mech.* **2001**, *100*, 77–96. [[CrossRef](#)]
22. Krieger, I.M. Rheology of monodisperse latices. *Adv. Colloid Interface Sci.* **1972**, *3*, 111–136. [[CrossRef](#)]
23. Briscoe, B.J.; Luckham, P.F.; Ren, S.R. The properties of drilling muds at high pressures and high temperatures. *Philos. Trans. R. Soc. Lond. A Math. Phys. Eng. Sci.* **1994**, *348*, 179–207. [[CrossRef](#)]
24. Maxwell, J.C. *A Treatise on Electricity and Magnetism*, 2nd ed.; Clarendon Press: Oxford, UK, 1873.
25. Hamilton, R.L.; Crosser, O.K. Thermal conductivity of heterogeneous two-component systems. *Ind. Eng. Chem. Fundam.* **1962**, *1*, 187–191. [[CrossRef](#)]
26. Jeffrey, D.J. Conduction through a random suspension of spheres. *Proc. R. Soc. Lond. A. Math. Phys. Sci.* **1973**, *335*, 355–367. [[CrossRef](#)]
27. Jaeger, J.C. Application of the theory of heat conduction to geothermal measurements. In *Terrestrial Heat Flow*; Lee, W.H.K., Ed.; Wiley Online Library: Hoboken, NJ, USA, 1965; pp. 7–23.
28. Agemar, T.; Weber, J.; Schulz, R. Deep geothermal energy production in Germany. *Energies* **2014**, *7*, 4397–4416. [[CrossRef](#)]

29. Phillips, R.J.; Armstrong, R.C.; Brown, R.A.; Graham, A.L.; Abbott, J.R. A constitutive equation for concentrated suspensions that accounts for shear-induced particle migration. *Phys. Fluids A Fluid Dyn.* **1992**, *4*, 30–40. [[CrossRef](#)]
30. Massoudi, M.; Antaki, J.F. An Anisotropic Constitutive Equation for the Stress Tensor of Blood Based on Mixture Theory. *Math. Probl. Eng.* **2008**, *2008*, 1–30. [[CrossRef](#)]
31. Massoudi, M. A Mixture Theory formulation for hydraulic or pneumatic transport of solid particles. *Int. J. Eng. Sci.* **2010**, *48*, 1440–1461. [[CrossRef](#)]
32. Soo, S. *Fluid Dynamics of Multiphase Systems*; Blaisdell Publishing Company: Waltham, MA, USA, 1967.
33. Wu, W.T.; Zhou, Z.F.; Aubry, N.; Antaki, J.F.; Massoudi, M. Heat transfer and flow of a dense suspension between two cylinders. *Int. J. Heat Mass Transf.* **2017**, *112*, 597–606. [[CrossRef](#)]
34. Rajagopal, K.R.; Tao, L. *Mechanics of Mixtures*; Series on Advances in Mathematics for Applied Sciences; World Scientific Publishers: Singapore, 1995.
35. Massoudi, M. A note on the meaning of mixture viscosity using the classical continuum theories of mixtures. *Int. J. Eng. Sci.* **2008**, *46*, 677–689. [[CrossRef](#)]
36. Wu, W.T.; Massoudi, M.; Yan, H. Heat Transfer and Flow of Nanofluids in a Y-Type Intersection Channel with Multiple Pulsations: A Numerical Study. *Energies* **2017**, *10*, 492. [[CrossRef](#)]
37. Slattery, J.C. *Advanced Transport Phenomena*; Cambridge University Press: Cambridge, UK, 1999.
38. Ounis, H.; Ahmadi, G.; McLaughlin, J.B. Brownian diffusion of submicrometer particles in the viscous sublayer. *J. Colloid Interface Sci.* **1991**, *143*, 266–277. [[CrossRef](#)]
39. Ounis, H.; Ahmadi, G.; McLaughlin, J.B. Dispersion and deposition of Brownian particles from point sources in a simulated turbulent channel flow. *J. Colloid Interface Sci.* **1991**, *147*, 233–250. [[CrossRef](#)]
40. Yang, H.; Aubry, N.; Massoudi, M. Heat transfer in granular materials: Effects of nonlinear heat conduction and viscous dissipation. *Math. Methods Appl. Sci.* **2013**, *36*, 1947–1964. [[CrossRef](#)]
41. Müller, I. On the entropy inequality. *Arch. Ration. Mech. Anal.* **1967**, *26*, 118–141. [[CrossRef](#)]
42. Ziegler, H. *An Introduction to Thermomechanics*, 2nd ed.; North-Holland Publishing Company: Amsterdam, The Netherlands, 1983.
43. Truesdell, C.; Noll, W. *The Nonlinear Field Theories of Mechanics*; Springer: Berlin, Germany, 1992.
44. Liu, I.S. *Continuum Mechanics*; Springer Science & Business Media: Berlin, Germany, 2002.
45. Carreau, P.J.; De Kee, D.; Chhabra, R.J. *Rheology of Polymeric Systems*; Hanser/Gardner Publications: Cincinnati, OH, USA, 1997.
46. Massoudi, M.; Phuoc, T.X. Remarks on constitutive modeling of nanofluids. *Adv. Mech. Eng.* **2012**. [[CrossRef](#)]
47. Phuoc, T.X.; Massoudi, M.; Chen, R.H. Viscosity and thermal conductivity of nanofluids containing multi-walled carbon nanotubes stabilized by chitosan. *Int. J. Therm. Sci.* **2011**, *50*, 12–18. [[CrossRef](#)]
48. Khan, N.U.; May, R. A generalized mathematical model to predict transient bottomhole temperature during drilling operation. *J. Pet. Sci. Eng.* **2016**, *147*, 435–450. [[CrossRef](#)]
49. Salehi, S.; Madani, S.A.; Kiran, R. Characterization of drilling fluids filtration through integrated laboratory experiments and CFD modeling. *J. Nat. Gas Sci. Eng.* **2016**, *29*, 462–468. [[CrossRef](#)]
50. Vajargah, A.K.; van Oort, E. Determination of drilling fluid rheology under downhole conditions by using real-time distributed pressure data. *J. Nat. Gas Sci. Eng.* **2015**, *24*, 400–411. [[CrossRef](#)]
51. Seifu, B.; Nir, A.; Semiat, R. Viscous dissipation rate in concentrated suspensions. *Phys. Fluids* **1994**, *6*, 3189–3191. [[CrossRef](#)]
52. Hsu, T.; Traykovski, P.A.; Kineke, G.C. On modeling boundary layer and gravity-driven fluid mud transport. *J. Geophys. Res. Oceans* **2007**, *112*. [[CrossRef](#)]
53. Van Rijn, L.C. Sediment Transport, Part II: Suspend load Transport. *J. Hydraul. Eng. ASCE* **1984**, *1104*, 1613–1641. [[CrossRef](#)]
54. Amoudry, L.; Hsu, T.; Liu, P. Schmidt number and near-bed boundary condition effects on a two-phase dilute sediment transport model. *J. Geophys. Res. Oceans* **2005**, *110*. [[CrossRef](#)]
55. Fourier, J. *The Analytical Theory of Heat*; Dover Publications: Mineola, NY, USA, 1955.
56. Winterton, R.H.S. Early study of heat transfer: Newton and Fourier. *Heat Transf. Eng.* **2001**, *22*, 3–11. [[CrossRef](#)]
57. Kaviany, M. *Principles of Heat Transfer in Porous Media*; Springer: New York, NY, USA, 1995.
58. Bashir, Y.M.; Goddard, J.D. Experiments on the conductivity of suspensions of ionically-conductive spheres. *AIChE J.* **1990**, *36*, 387–396. [[CrossRef](#)]

59. Prasher, R.S.; Koning, P.; Shipley, J.; Devpura, A. Dependence of thermal conductivity and mechanical rigidity of particle-laden polymeric thermal interface material on particle volume fraction. *J. Electron. Packag.* **2003**, *125*, 386–391. [[CrossRef](#)]
60. Lee, D.L.; Irvine, T.F., Jr. Shear rate dependent thermal conductivity measurements of non-Newtonian fluids. *Exp. Therm. Fluid Sci.* **1997**, *15*, 16–24. [[CrossRef](#)]
61. Tominaga, Y.; Stathopoulos, T. Turbulent Schmidt numbers for CFD analysis with various types of flowfield. *Atmos. Environ.* **2007**, *41*, 8091–8099. [[CrossRef](#)]
62. Reynolds, A.J. The prediction of turbulent Prandtl and Schmidt numbers. *Int. J. Heat Mass Transf.* **1975**, *18*, 1055–1069. [[CrossRef](#)]
63. Batchelor, G.K.; O'Brien, R.W. Thermal or electrical conduction through a granular material. *Proc. R. Soc. Lond. A. Math. Phys. Sci.* **1977**, *355*, 313–333. [[CrossRef](#)]
64. Wang, X.Q.; Mujumdar, A.S. Heat transfer characteristics of nanofluids: A review. *Int. J. Therm. Sci.* **2007**, *46*, 1–19. [[CrossRef](#)]
65. Touloukian, Y.S.; Powell, R.W.; Ho, C.Y.; Nicolaou, M.C. *Thermophysical Properties of Matter—The TPRC Data Series. Volume 10. Thermal Diffusivity*; DTIC Document: Bedford, MA, USA, 1974.
66. Pope, S.B. *Turbulent Flows*; IOP Publishing: Bristol, UK, 2000.
67. Wilcox, D.C. Formulation of the kw turbulence model revisited. *AIAA J.* **2008**, *46*, 2823–2838. [[CrossRef](#)]
68. Jones, W.P.; Launder, Be. The prediction of laminarization with a two-equation model of turbulence. *Int. J. Heat Mass Transf.* **1972**, *15*, 301–314. [[CrossRef](#)]
69. OpenCFD. *OpenFOAM Programmer's Guide Version 2.1.0*; OpenCFD, Ed.; Free Software Foundation, Inc.: Boston, MA, USA, 2011.
70. Wu, W.T.; Yang, F.; Antaki, J.F.; Aubry, N.; Massoudi, M. Study of blood flow in several benchmark micro-channels using a two-fluid approach. *Int. J. Eng. Sci.* **2015**, *95*, 49–59. [[CrossRef](#)] [[PubMed](#)]
71. Rusche, H. *Computational Fluid Dynamics of Dispersed Two-Phase Flows at High Phase Fractions*; Imperial College London (University of London): London, UK, 2002.
72. Ubbink, O. Numerical Prediction of Two Fluid Systems with Sharp Interfaces. Ph.D. Thesis, University of London, London, UK, January 1997.
73. Kim, J. Multiphase CFD Analysis and Shape-Optimization of Blood-Contacting Medical Devices. Ph.D. Thesis, Carnegie Mellon University, Pittsburgh, PA, USA, 2012.
74. *ICEM CFD*, version 14.0; ANSYS Inc.: Canonsburg, PA, USA, 2012.
75. Yilmazer, B. Investigation of some physical and mechanical properties of concrete produced with barite aggregate. *Sci. Res. Essays* **2010**, *5*, 3826–3833.
76. Tetlow, N.; Graham, A.L.; Ingber, M.S.; Subia, S.R.; Mondy, L.A.; Altobelli, S.A. Particle migration in a Couette apparatus: Experiment and modeling. *J. Rheol.* **1998**, *42*, 307–327. [[CrossRef](#)]
77. Akhshik, S.; Behzad, M.; Rajabi, M. CFD–DEM approach to investigate the effect of drill pipe rotation on cuttings transport behavior. *J. Pet. Sci. Eng.* **2015**, *127*, 229–244. [[CrossRef](#)]
78. Siginer, D.A.; Bakhtiyarov, S.I. Flow of drilling fluids in eccentric annuli. *J. Nonnewton. Fluid Mech.* **1998**, *78*, 119–132. [[CrossRef](#)]
79. Wu, W.T.; Aubry, N.; Massoudi, M.; Kim, J.; Antaki, J.F. A numerical study of blood flow using mixture theory. *Int. J. Eng. Sci.* **2014**, *76*, 56–72. [[CrossRef](#)] [[PubMed](#)]
80. Massoudi, M.; Kim, J.; Antaki, J.F. Modeling and numerical simulation of blood flow using the theory of interacting continua. *Int. J. Non Linear Mech.* **2012**, *47*, 506–520. [[CrossRef](#)] [[PubMed](#)]
81. Bednarz, A.; Weber, B.; Jupke, A. Development of a CFD model for the simulation of a novel multiphase counter-current loop reactor. *Chem. Eng. Sci.* **2017**, *161*, 350–359. [[CrossRef](#)]
82. Das, D.; Samal, D.P.; Mohammad, N.; Meikap, B.C. Hydrodynamics of a multi-stage counter-current fluidized bed reactor with down-comer for amine impregnated activated carbon particle system. *Adv. Powder Technol.* **2017**, *28*, 854–864. [[CrossRef](#)]
83. Garić-Grulović, R.; Radoičić, T.K.; Arsenijević, Z.; Đuriš, M.; Grbavčić, Ž. Hydrodynamic modeling of downward gas–solids flow. Part I: Counter-current flow. *Powder Technol.* **2014**, *256*, 404–415. [[CrossRef](#)]

